

Ozone Production in the Positive DC Corona Discharge: Model and Comparison to Experiments

Junhong Chen¹ and Jane H. Davidson^{1,2}

Received January 24, 2002; revised March 11, 2002

A numerical model of ozone generation in clean, dry air by positive DC corona discharges from a thin wire is presented. The model combines the physical processes in the corona discharge with the chemistry of ozone formation and destruction in the air stream. The distributions of ozone and nitrogen oxides are obtained in the neighborhood of the corona discharge wire. The model is validated with previously published experimental data. About 80% of the ozone produced is attributed to the presence of excited nitrogen and oxygen molecules. A parametric study reveals the effects of linear current density (0.1–100 $\mu\text{A}/\text{cm}$ of wire), wire radius (10–1000 μm), temperature (300–800 K) and air velocity (0.05–2 m/s) on the production of ozone. The rate of ozone production increases with increasing current and wire size and decreases with increasing temperature. The air velocity affects the distribution of ozone, but does not affect the rate of production.

KEY WORDS: Corona discharge; corona plasma; ozone; electrostatic precipitator; NO_x .

1. INTRODUCTION

Recognition of the health risks of breathing ozone^(1–5) has led to stringent regulations for ambient concentration,⁽⁶⁾ standards for levels in the workplace,⁽⁷⁾ and limits for devices that produce ozone indoors.⁽⁸⁾ Ozone is produced by devices like electronic air cleaners, laser printers and copiers, which rely on atmospheric corona discharges. On the other hand, the oxidative properties of ozone have been harnessed for beneficial purposes such as water treatment and odor and color control.^(9–12) In these applications, ozone is almost always produced at high rates in dielectric barrier discharges in pure oxygen.

Both experimental and numerical studies have been conducted to improve ozone production rates in oxygen.^(13–20) Eliasson *et al.*⁽¹³⁾ provided the most detailed model of ozone production in dielectric barrier discharges

¹Department of Mechanical Engineering, University of Minnesota, Minneapolis, MN 55455.

²To whom all correspondence should be addressed.

and emphasized the importance of including the excited molecular states in the chemistry of ozone formation.

The generation of ozone in air is more complicated than that in pure oxygen due to the presence of nitrogen and water vapor. Experimental studies^(21–29) have considered the dependence of the ozone generation on the discharge polarity, current level, electrode size, temperature, air velocity, and relative humidity. However, models of ozone generation by corona discharges in air are limited and do not accurately account for the spatial number density distributions and energy distributions of electrons or the contribution of excited oxygen and nitrogen species.^(17,30,31) Both excited O_2 (O_2^*) and excited N_2 (N_2^*) are expected to contribute to the ozone production.^(13,27,32–43) Yagi and Tanaka⁽³¹⁾ and Peyrou⁽¹⁷⁾ modeled ozone generation in pulse discharges. Both models used an average electron density and spatially independent rate coefficients to calculate the rate of electron-impact reactions. Naidis⁽³⁰⁾ approximated the spatial distribution of electrons in DC corona discharges using empirical expressions for the rate coefficients of electron-impact reactions as functions of electric field. The highly simplified chemistry model included one excited nitrogen state; the dissociation of O_2 by electrons and metastable $N_2(A\ ^3\Sigma_u^+)$ molecules (assuming that 70% of O_2 is disassociated in the reaction with $N_2(A)$) was followed by the three-body reaction ($O + O_2 + M = O_3 + M$) to form ozone. The contributions of the excited states of O_2 and other excited states of N_2 were neglected.

In this paper, a comprehensive numerical model of ozone production in clean, dry air at one atmosphere by a positive, DC corona discharge from a thin wire is described. It is used to determine distributions of ozone and other gaseous products including O, N, NO, N_2O , NO_2 , NO_3 , N_2O_5 , O_2^* , and N_2^* . Numerical results are compared to published experimental data. A parametric study is conducted to examine the effects of linear current density (0.1–100 μA per cm of wire length), wire radius (10–1000 μm), air temperature (300–800 K), and air velocity (0.05–2 m/s) on the distribution of ozone.

2. NUMERICAL MODEL

The numerical model combines the physical processes in a positive DC corona discharge surrounding a wire discharge electrode with the chemistry of ozone formation and destruction in the air stream moving transverse to the wire. The model has three parts: a model of the corona plasma, a model of the chemistry, and a transport model. The electron number density and kinetic energy distributions determined in the plasma model are used to calculate the electron-impact reaction rates. The chemistry model includes

reactions pertinent to ozone generation in the atmosphere including those involving excited molecules. The transport model, developed within the framework of the commercial software FLUENT[®] (version 5.5),⁽⁴⁴⁾ solves the conservation of mass, momentum and energy equations and the species transport equations for two-dimensional laminar flow. The reaction rates determined from the corona plasma and chemistry models are included as a source term in the species transport equations.

2.1. Computational Domain

The computational domain for the wire-plate geometry is shown in Fig. 1. The high-voltage wire electrode is suspended equidistant from two parallel plane walls. Airflow is transverse to the wire. High-energy electrons that initiate the chemical reactions are produced in a very small ionization region surrounding the wire. For positive discharges, the plasma region is uniform along the wire and thus the electron distribution can be approximated as one-dimensional in the radial direction.

In this model, we assume that the inlet airflow is uniform with velocity U in the streamwise (x) direction. The flow is modeled as steady, two-dimensional, and laminar. The effect of the electric body force on the gas flow is neglected. The electric body force within the corona plasma does not generate vorticity because within that small region the discharge is assumed to be 1-D in the radial direction and the contours of constant space charge density are normal to the electric field lines.⁽⁴⁵⁾ Any electrically induced turbulence

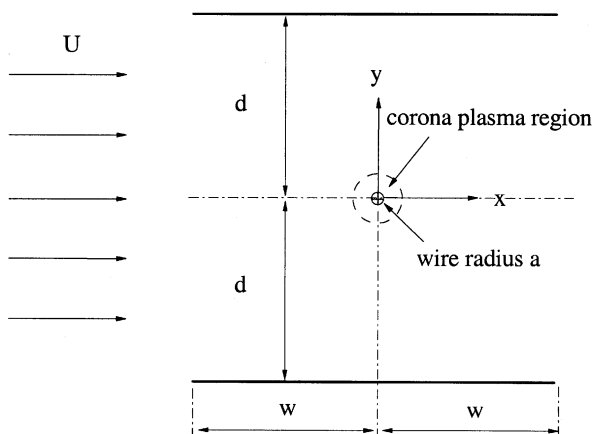


Fig. 1. The computational domain for a corona discharge along a wire is shown. The dashed line indicates the outside boundary of the corona plasma.

would be outside the ionization region and thus would not affect ozone production rates or the distribution of ozone near the wire.

The wire-plate spacing (d) and the half-width of the plates (w) were chosen as small as possible to minimize computation time. The criterion for the wire-plate spacing is that d is large enough so that neither the flow field nor the diffusion of ozone is affected by the presence of the plates. For the cases considered in this paper, a wire-plate spacing equal to five times the plasma thickness was sufficient. Plasma thickness increases with increasing wire radius and air temperature but is independent of current and potential.⁽⁴⁶⁾

The electron-impact reactions primarily occur in the corona plasma region. However, radicals (e.g., O, N, O₂^{*}, and N₂^{*}) produced by electron-impact reactions may be transported outside of the plasma region by convection and diffusion. These radicals contribute to the formation of ozone outside the plasma region. However, the dominant mechanism outside the corona plasma is the destruction of ozone. Thus, the overall production rate at the exit of a specific device depends on the total residence time in the device. The plate half-width (w) and mean air velocity (U) determine the residence time. The residence time may be less than the time to reach chemical equilibrium. Most indoor electronic air cleaners operate with a residence time of 10 to 20 ms. Results from the present model indicate that for a current density of 2.55 $\mu\text{A}/\text{cm}$ (typical of many corona devices), ozone production rate is constant for residence times between 0.75 and 30 ms. As discussed in Section 3.1, the insensitivity of the ozone production rate to realistic variations in residence time is expected, based on estimated characteristic times for the formation and destruction reactions of ozone in air. For the range of velocities considered here, a plate half-width equal to 0.15 cm is used.

2.2. Corona Plasma Model

Corona discharge occurs when the voltage applied to the thin electrode is high enough to ionize the gaseous species surrounding the discharge electrode. The minimum electric field required for the corona discharge in dry air is estimated by Peek's equation⁽⁴⁷⁾ and is a function of the electrode size, the surface roughness of the electrode, temperature, and pressure. The corona plasma region is bounded by the electrode surface and the ionization boundary where the rate of ionization balances the rate of the electron attachment. This balance exists at a reduced electric field (E/N , where N is the neutral density) of 120 Td ($1 \text{ Td} = 10^{-21} \text{ V m}^2$).⁽⁴⁸⁾ For example, at one atmosphere and 293 K, the electric field at the outside edge of the plasma is 30 kV/cm. At a fixed temperature and pressure, the thickness of the corona

plasma is only a function of the radius of curvature of the discharge electrode. The voltage potential affects only the electron number density. Within the plasma region, the ionization process that produces electrons prevails over the attachment of electrons to the electronegative gas molecules. Outside the plasma, attachment prevails over ionization. Ions of the same polarity as the discharge electrode that drift into this region carry the current. Electrons produced in the corona discharge initiate and drive the gas-phase reactions. The rate of electron-impact reactions depends on the electron number density and the electron kinetic energy. In an earlier paper,⁽⁴⁶⁾ we describe the details of the corona plasma model and present results for air at 293 K. Here we briefly summarize the modeling approach, discuss the effects of variations in air temperature, and use the relevant results to calculate rate coefficients for electron-impact reactions.

The electron number density and electric field are determined from solutions of the coupled charge carrier (electrons and ions) continuity equations and the simplified Maxwell's equation. The operating current establishes the number density of electrons at the wire surface. In this paper, current is expressed as either a linear current density (I) given in units of current per unit length of wire or as surface current density (J) given in units of current per surface area of the wire. The electron kinetic energy distribution is obtained by solving the spatially homogeneous Boltzmann equation, taking into account 39 electron-impact reactions in air.

The corona plasma occupies a small region (about 2 to 10 wire radii depending on wire size) surrounding the discharge wire. For a fixed wire radius, the plasma thickness increases with increasing temperature and decreasing pressure. The number of electrons increases with increasing current and wire radius. It is a weak function of air temperature. The non-Maxwellian distribution of electron energy depends solely on the reduced electric field. The mean kinetic energy of electrons increases with the increase of the reduced field. Consequently, it decreases with increasing wire radius, but is insensitive to changes in current.

With the increase of temperature, the corona plasma expands and the mean free path of electrons increases. As a result, inelastic collisions to produce electrons become less frequent and fewer electrons are produced. Electrons tend to absorb more energy from the electric field between collisions. The electron number density and the electron mean kinetic energy are plotted as a function of temperature and distance from the wire surface in Figs. 2 and 3, respectively. Both decrease with increasing distance from the wire surface. From 300 to 800 K, the total number of electrons decreases by 10%. Figure 3 shows that electrons are more energetic and the plasma region expands with increasing temperature. The thickness of the corona plasma is

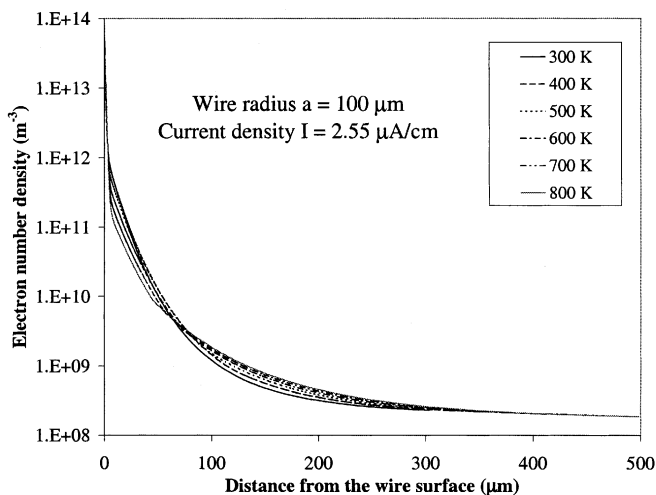


Fig. 2. Effect of gas temperature on electron number density distribution for a positive corona discharge from a $100\text{ }\mu\text{m}$ -radius wire operated with a linear current density of $2.55\text{ }\mu\text{A/cm}$.

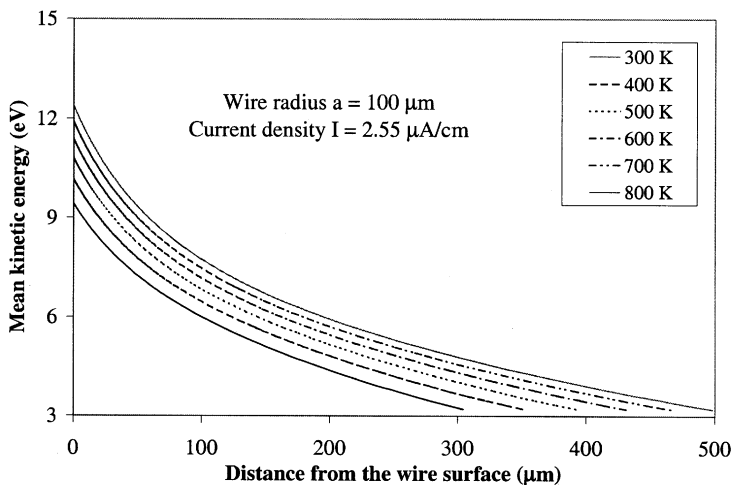


Fig. 3. Effect of gas temperature on the mean kinetic energy of electrons for a $100\text{ }\mu\text{m}$ -radius wire with a linear current density of $2.55\text{ }\mu\text{A/cm}$. The thickness of the corona plasma is indicated by the termination of the curves along the abscissa. For example, at 300 K , the corona plasma extends $304\text{ }\mu\text{m}$ beyond the surface of the wire.

indicated by the termination of the curves along the abscissa. At 300 K, the plasma thickness is 304 μm . At 800 K, the thickness is 498 μm .

The rate coefficient (k_e) for an electron-impact reaction is given by

$$k_e = \int_{u_{\text{th}}}^{\infty} \sqrt{\frac{2eu}{m_e}} \sigma(u) f_0(u) u^{1/2} du \quad (1)$$

where u is the kinetic energy of electrons, u_{th} is the energy threshold for the reaction (e.g., the measured value of u_{th} is 5.1 eV for dissociation of O_2 ⁽⁴⁹⁾), e is the elementary charge, m_e is the electron mass, $\sigma(u)$ is the electron-impact collision cross-section, which is a function of electron energy, and $f_0(u)$ is the electron kinetic energy distribution function. Thus, like the electron energy distribution, the rate coefficients for electron-impact reactions depend solely on the reduced electric field. As an example, Fig. 4 shows a distribution of rate coefficients for the dissociation of O_2 , N_2 , and O_3 , and the excitation of O_2 and N_2 for wire radius $a = 100 \mu\text{m}$, linear current density $I = 2.55 \mu\text{A}/\text{cm}$ and air temperature $T = 300 \text{ K}$. Although there are inconsistencies in the threshold energy for the dissociation of O_2 in the literature,^(32,49) the electron-impact dissociation cross-sections used in the model are for electron kinetic energy higher than 8 eV.⁽⁵⁰⁾ The rate coefficients decrease exponentially with increasing distance from the wire surface

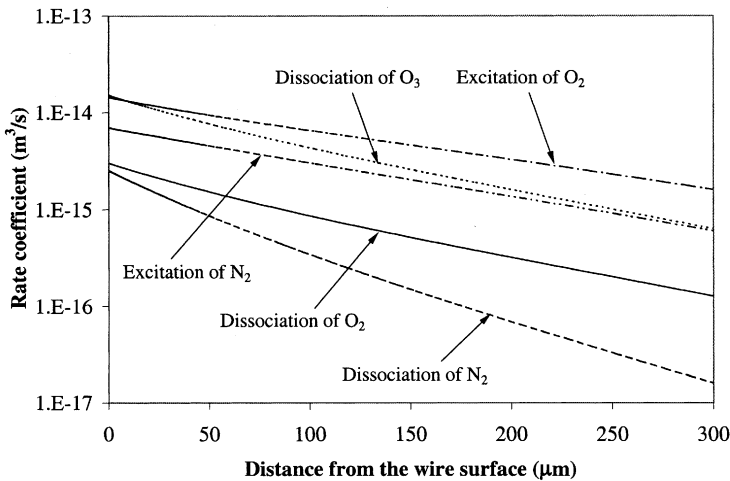


Fig. 4. Rate coefficients as a function of distance from the surface of the discharge wire are plotted for electron-impact reactions in the positive DC corona discharge at 300 K. The wire radius is 100 μm and the operating linear current density is 2.55 $\mu\text{A}/\text{cm}$.

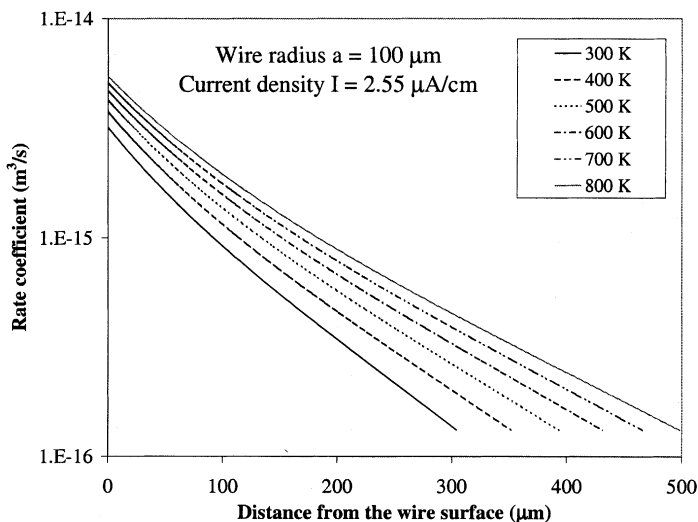


Fig. 5. Effect of temperature on the rate coefficient of electron-impact dissociation of O_2 for a $100 \mu\text{m}$ -radius wire with a linear current density of $2.55 \mu\text{A/cm}$.

due to the decrease of the electric field. The rate coefficients for electron-impact reactions increase with increasing temperature. To illustrate the temperature dependence, the rate coefficient for electron-impact dissociation of O_2 is plotted for temperatures from 300 to 800 K in Fig. 5.

2.3. Chemistry Model

All models of ozone production in plasmas use a subset of the gas-phase reactions of neutral species in the earth's atmosphere. The kinetics and photochemistry of gas-phase chemical reactions in the atmosphere have been tabulated^(51–54) and are updated regularly.^(55–57) The reactions and the corresponding Arrhenius rate coefficients included in this model are listed in Table I. They include 12 neutral species and 24 reactions, including 5 electron-impact reactions (1e through 5e) and 19 neutral reactions (6 to 24) including those of O_2^* and N_2^* (22 to 24). Reactions (6), (7), and (22) contribute directly to the formation of ozone.

An important modification to previous models of ozone generation in corona discharges is the inclusion of reactions involving N_2^* and O_2^* (reactions 4e, 5e, 22, 23, and 24). In addition, the rate coefficients are updated to reflect the values in the recent atmospheric chemistry models.^(42,55,56,58) The selection of reactions was based on the following criteria. Reactions

Table I. Proposed Reaction Mechanisms for Ozone Production in Positive Corona Discharges in Dry Air

No.	Reaction	Rate coefficient ($\text{cm}^3 \cdot \text{mol}^{-1} \cdot \text{s}^{-1}$)	Reference
1e	$e + \text{O}_2 = \text{O} + \text{O} + e$	k_{1e}	Eq. (1)
2e	$e + \text{N}_2 = \text{N} + \text{N} + e$	k_{2e}	Eq. (1)
3e	$e + \text{O}_3 = \text{O} + \text{O}_2 + e$	$5 \sim 10 k_{1e}$	43
4e	$e + \text{O}_2 = \text{O}_2^* + e$	k_{4e}	Eq. (1)
5e	$e + \text{N}_2 = \text{N}_2^* + e$	k_{5e}	Eq. (1)
6	$\text{O} + \text{O}_2 + \text{O}_2 = \text{O}_3 + \text{O}_2$	$6.0 \times 10^{-34} (T/300)^{-2.8} [\text{O}_2]$	56
7	$\text{O} + \text{O}_2 + \text{N}_2 = \text{O}_3 + \text{N}_2$	$5.6 \times 10^{-34} (T/300)^{-2.8} [\text{N}_2]$	56
8	$\text{O} + \text{O}_3 = \text{O}_2 + \text{O}_2$	$8.0 \times 10^{-12} \exp(-2060/T)$	56
9	$\text{O} + \text{NO} + \text{N}_2 = \text{NO}_2 + \text{N}_2$	$1.0 \times 10^{-31} (T/300)^{-1.6} [\text{N}_2]$	56
10	$\text{O} + \text{NO}_2 = \text{NO} + \text{O}_2$	$5.6 \times 10^{-12} \exp(180/T)$	55
11	$\text{O} + \text{NO}_3 = \text{O}_2 + \text{NO}_2$	1.7×10^{-11}	56
12	$\text{O} + \text{N}_2\text{O}_5 = \text{NO}_2 + \text{NO}_2 + \text{O}_2$	1.0×10^{-16}	58
13	$\text{N} + \text{O}_2 = \text{NO} + \text{O}$	$1.5 \times 10^{-11} \exp(-3600/T)$	58
14	$\text{N} + \text{O}_3 = \text{NO} + \text{O}_2$	1.0×10^{-16}	43
15	$\text{N} + \text{NO} = \text{N}_2 + \text{O}$	$2.1 \times 10^{-11} \exp(100/T)$	58
16	$\text{N} + \text{NO}_2 = \text{N}_2\text{O} + \text{O}$	$5.8 \times 10^{-12} \exp(220/T)$	58
17	$\text{NO} + \text{O}_3 = \text{NO}_2 + \text{O}_2$	$3.0 \times 10^{-12} \exp(-1500/T)$	55
18	$\text{NO} + \text{NO}_3 = 2\text{NO}_2$	$1.8 \times 10^{-11} \exp(110/T)$	56
19	$\text{NO}_2 + \text{O}_3 = \text{NO}_3 + \text{O}_2$	$1.4 \times 10^{-13} \exp(-2470/T)$	56
20	$\text{NO}_2 + \text{NO}_3 + \text{N}_2 = \text{N}_2\text{O}_5 + \text{N}_2$	$2.8 \times 10^{-30} (T/300)^{-3.5} [\text{N}_2]$	56
21	$\text{N}_2\text{O}_5 + \text{N}_2 = \text{NO}_2 + \text{NO}_3 + \text{N}_2$	$1.0 \times 10^{-3} (T/300)^{-3.5} \exp(-11,000/T) [\text{N}_2]$	56
22	$\text{O}_2^* + \text{O}_2 = \text{O}_3 + \text{O}$	4.8×10^{-15}	33
23	$\text{N}_2^* + \text{O}_2 = \text{N}_2 + 2\text{O}$	$3.0 \times 10^{-12} (T/300)^{0.55}$	36,41
24	$\text{N}_2^* + \text{O}_2 = \text{N}_2\text{O} + \text{O}$	$6.0 \times 10^{-14} (T/300)^{0.55}$	35

with rate coefficients greater than $10^{-11} \text{ cm}^3 \text{ mol}^{-1} \text{ s}^{-1}$ are included. Reactions with lower rate coefficients are neglected unless they involve one of the more prevalent species such as N_2 , O_2 , O_3 , O , N , and NO . Because of the relatively low concentrations of O^* and N^* , the model assumes that their rate coefficients are identical to those of the ground state atoms. Ionic species do not have sufficient energy to dissociate O_2 and thus are not included.

Usually electronically excited states of molecules are short-lived with a lifetime on the order of 10^{-8} s .⁽⁵⁹⁾ Only those excited species with high-energy and a relatively long lifetime (on the order of magnitude of the characteristic time of a reaction to dissociate O_2) contribute to the formation of ozone. In this model, excited states of O_2 considered include $\text{O}_2(A^3\Sigma_u^+)$, $\text{O}_2(A'^3\Delta_u)$, $\text{O}_2(c^1\Sigma_u^-)$, and $\text{O}_2(B^3\Sigma_u^-)$. Excited states of N_2 include $\text{N}_2(A^3\Sigma_u^+)$, $\text{N}_2(B^3\Pi_g)$, $\text{N}_2(W^3\Delta_u)$, $\text{N}_2(B'^3\Sigma_u^-)$, $\text{N}_2(a^1\Sigma_u^-)$, $\text{N}_2(a^1\Pi_g)$, and $\text{N}_2(w^1\Delta_u)$. Because only limited rate coefficients are available in the literature, the same rate coefficient is assumed for different excited states of N_2 or O_2 (see Table I).

Reaction (22) between the excited O_2 and ground state O_2 to form O_3 was first proposed by Benson⁽⁶⁰⁾ and then further studied by Sugimitsu and Okazaki.⁽³³⁾ The excitation energy of O_2 must be greater than 4.1 eV for this reaction to proceed. Excited O_2 states that could possibly contribute to this reaction are $A^3\Sigma_u^+$, $A'^3\Delta_u$, $c^1\Sigma_u^-$ and $B^3\Sigma_u^-$.⁽⁶¹⁾ No direct measurement of the rate coefficient for reaction (22) is available. The value used in this model is inferred from measurements of ozone generation in oxygen by Sugimitsu and Okazaki.⁽³³⁾

The excited metastable species $N_2(A^3\Sigma_u^+)$ has a lifetime of 1.3–2.6 s.⁽⁶²⁾ It is highly reactive and its importance in the overall kinetics of dielectric barrier discharges in pure N_2 and N_2 – O_2 was shown by Guerra and Loureiro.⁽³⁸⁾ The reactions between $N_2(A^3\Sigma_u^+)$ and O_2 are the most extensively studied reactions among the excited states of N_2 and recently have been incorporated into the chemical kinetic scheme for non-thermal air plasma chemistry.⁽⁴²⁾ The measured rate coefficients for $N_2(A^3\Sigma_u^+, v=0)$, $N_2(A^3\Sigma_u^+, v=1)$, and $N_2(A^3\Sigma_u^+, v=2)$ are 2.5×10^{-12} , 4×10^{-12} , and $4.5 \times 10^{-12} \text{ cm}^3 \text{ mol}^{-1} \text{ s}^{-1}$, respectively.^(36,37) The temperature dependence of the rate coefficient is $T^{0.55}$.⁽³⁶⁾ We did not differentiate these vibrationally excited species but took them into account by assuming a slightly higher rate ($3 \times 10^{-12} \text{ cm}^3 \text{ mol}^{-1} \text{ s}^{-1}$) than the most populated state $N_2(A^3\Sigma_u^+, v=0)$. There are two primary product channels for this reaction: one to produce ground state N_2 and O (reaction 23) and the other to produce N_2O and O (reaction 24).^(32,35,36,41) The branching ratio of this reaction leading to N_2O production is between 1 and 4%. We used 2%.

The excited metastable species $N_2(a^1\Sigma_u^-)$ (lifetime 0.017–0.5 s) and $N_2(a^1\Pi_g)$ have relatively long lifetimes⁽⁵⁹⁾ and sufficient energy to dissociate O_2 and thus contribute to the formation of ozone. $N_2(a^1\Sigma_u^-)$ has been found to be important for discharge chemistry.^(40,43) Excited triplet states $N_2(B^3\Pi_g)$ contribute to the dissociation of O_2 .^(34,38,43) Eliasson and Kogelschatz⁽³⁹⁾ point out that $N_2(W^3\Delta_u)$ and $N_2(B'^3\Sigma_u^-)$ can quickly cascade to the metastable $N_2(A^3\Sigma_u^+)$ state by photon emission and collisions. Consequently, these two excited species are included. $N_2(w^1\Delta_u)$, considered by Braun *et al.*⁽⁴⁰⁾ and Guerra *et al.*,⁽³⁸⁾ is also included.

2.4. Transport Model

In this model, the distributions of ozone as well as other species including O, N, NO, N_2O , NO_2 , NO_3 , N_2O_5 , O_2^* , and N_2^* are obtained. The governing equations are the conservation equations of mass, momentum, energy, and individual species continuity equations for 2-D, incompressible, steady state, and laminar flow. The simplified continuity and momentum

equations are

$$\frac{\partial v_i}{\partial x_i} = 0 \quad (2)$$

and

$$\rho \frac{\partial}{\partial x_j} (v_i v_j) = -\frac{\partial p}{\partial x_i} + \frac{\partial}{\partial x_j} \left(\mu \left(\frac{\partial v_i}{\partial x_j} + \frac{\partial v_j}{\partial x_i} \right) \right) + \rho g_i \quad (3a)$$

where ρ is the density of an ideal gas mixture, p is the pressure, v_i is the air velocity, i and j are spatial indices for a Cartesian coordinate system, μ is the dynamic viscosity of the mixture and ρg_i is the gravitational body force. At the inlet, velocity is assumed to be uniform in the x -direction,

$$v_x|_{x=-w} = U \quad \text{and} \quad v_y|_{x=-w} = 0 \quad (3b)$$

The conditions of the outflow plane are extrapolated from within the domain and have no impact on the upstream flow. The extrapolation procedure updates the outflow velocity and pressure consistent with a fully developed flow assumption,

$$\frac{\partial v_x}{\partial x} \Big|_{x=w} = \frac{\partial v_y}{\partial x} \Big|_{x=w} = 0 \quad (3c)$$

Along the x -axis, symmetry boundary conditions are specified,

$$\frac{\partial v_x}{\partial y} \Big|_{y=0} = \frac{\partial v_y}{\partial y} \Big|_{y=0} = \frac{\partial p}{\partial y} \Big|_{y=0} = 0 \quad (3d)$$

On the plates and the surface of the wire, no-slip velocity boundary conditions are specified,

$$v_x|_{x=\pm d} = v_y|_{x=\pm d} = 0 \quad \text{and} \quad v_x|_{r=\sqrt{x^2+y^2}=a} = v_y|_{r=\sqrt{x^2+y^2}=a} = 0 \quad (3e)$$

The species transport equation is,

$$\rho \frac{\partial}{\partial x_i} (v_i m_{j'}) = -\frac{\partial}{\partial x_i} J_{j'i} + R_{j'} \quad (4a)$$

where $m_{j'}$ is the local mass fraction of the species j' , $J_{j'i}$ is the dilute diffusion flux of species j' and the source term $R_{j'}$ is the volumetric rate of creation/depletion of species j' by chemical reactions, including neutral reactions and electron-impact reactions. Rates of neutral reactions are calculated using the rate coefficients listed in Table I. The electron-impact reaction rates are calculated as described in Section 2.2. The dilute diffusion flux of species

j' is

$$J_{j'i} = -\rho D_j \frac{\partial m_{j'}}{\partial x_i} \quad (4b)$$

where D_j is the dilute diffusion coefficient for species j' in air. Thermal diffusion of species is neglected. An equation of the form (4a) is solved for $L-1$ species where L is the total number of chemical species present in the system ($L = 12$ for this case). The mass fraction of the last species (N_2) is given by the constraint,

$$\sum_{j'} m_{j'} = 1 \quad (4c)$$

Four boundary conditions are required for each species. At the inlet, air is assumed to consist of 21% O_2 and 79% N_2 ; the mass fractions of O_2 and N_2 are 0.233 and 0.767 respectively. The mass fraction for all other species is assumed equal to zero. At the outlet, a zero diffusion flux is assumed,

$$\left. \frac{\partial m_{j'}}{\partial x} \right|_{x=w} = 0 \quad (4d)$$

A symmetry condition is assumed for all species concentrations,

$$\left. \frac{\partial m_{j'}}{\partial y} \right|_{y=0} = 0 \quad (4e)$$

At wall boundaries, there is no penetration, evaporation or chemical reactions involving inactive species. Reactions of active species (O , N , O_2^* , N_2^* , and O_3) with the surface are neglected:

$$\left. \frac{\partial m_{j'}}{\partial y} \right|_{y=\pm d} = \left. \frac{\partial m_{j'}}{\partial r} \right|_{r=\sqrt{x^2+y^2}=a} = 0 \quad (4f)$$

The simplified energy equation is

$$\rho \frac{\partial}{\partial x_i} (c_p v_i T) = \frac{\partial}{\partial x_i} \left(\lambda \frac{\partial T}{\partial x_i} - \sum_{j'} h_{j'} J_{j'i} \right) + \sum_{j'} \left(\frac{h_{j'}^0}{M_{j'}} R_{j'} \right) \quad (5a)$$

where c_p is the specific heat of the mixture at constant pressure, λ is the thermal conductivity of the mixture, $h_{j'}$ is the specific enthalpy of species j' , $h_{j'}^0$ is the formation enthalpy of species j' at the reference temperature 298.15 K and $M_{j'}$ is the molecular weight of species j' . The first term on the right-hand side of Eq. (5a) represents energy transfer due to conduction and species diffusion. The second term represents the heat addition by chemical reactions. Joule heating is neglected. For a linear current density of

2.55 $\mu\text{A}/\text{cm}$ and an air velocity of 1 m/s, the temperature rise in the computational domain due to the Joule heating is estimated as 0.4°C. For the maximum current density (100 $\mu\text{A}/\text{cm}$) considered in this paper, the temperature rise is about 16°C. The local temperature rise may be higher in the vicinity of the wire. As shown in our results, the rate of ozone production is a weak function of temperature. Thus, the neglect of Joule heating is justified. Four boundary conditions for temperature are specified at the inlet, outlet, x -axis and wall boundaries. A uniform temperature T_0 is known at the inlet,

$$T|_{x=-w} = T_0 \quad (5b)$$

At the outlet, a zero heat flux is assumed,

$$\left. \frac{\partial T}{\partial x} \right|_{x=w} = 0 \quad (5c)$$

A symmetry boundary condition also applies to temperature,

$$\left. \frac{\partial T}{\partial y} \right|_{y=0} = 0 \quad (5d)$$

Adiabatic boundary conditions are assumed on the plates and the surface of the wire,

$$\left. \frac{\partial T}{\partial y} \right|_{y=\pm d} = 0 \quad \text{and} \quad \left. \frac{\partial T}{\partial r} \right|_{r=\sqrt{x^2+y^2}=a} = 0 \quad (5e)$$

Model results show that the heat release from chemical reactions is negligible. As a result, one can obtain accurate results by assuming the gas is isothermal.

2.5. Thermodynamic and Transport Properties

Thermodynamic data for individual species are obtained from the NIST-JANAF thermochemical table⁽⁶³⁾ and then curve-fit as a fourth-order polynomial function of temperature. Transport properties of individual species are calculated from the Chapman–Enskog kinetic theory⁽⁶⁴⁾ using the TRANSPORT package of Chemkin-III software⁽⁶⁵⁾ and then curve-fit as a third-order polynomial function of temperature. The thermodynamic and transport properties of excited species are assumed to be the same as their corresponding ground-state species. The specific heat of the mixture c_p is calculated using the mixing law based on mass fraction. The viscosity μ and the thermal conductivity λ of the mixture are calculated using the ideal gas mixing law.

2.6. Numerical Implementation

The computation is divided into two parts: the computation for the electron number density and the electron energy distributions,⁽⁴⁶⁾ and the computation of the flow field and the species concentration distribution. The computed electron distribution is used to calculate the reaction rate for the electron-impact reactions. Conservation equations (Eqs. 2 to 5), together with the necessary boundary conditions are solved in FLUENT[®].

The computational domain was meshed into triangular elements with finer meshes close to the wire surface where the chemical reactions occur. During the solution process, the mesh close to the wire surface was adapted to increasingly finer meshes to test the dependence of the results on mesh size. The adaptation process was terminated when the final results did not change with further refinement. The minimum area of the mesh (close to the wire surface) is $1.4 \times 10^{-12} \text{ m}^2$. The largest mesh (close to the plates and near the inlet and outlet) is $8.8 \times 10^{-10} \text{ m}^2$. The total number of cells in the computational domain varied from 10^5 to 10^6 .

The momentum equation, energy equation, and species transport equations were discretized using the first order upwind scheme and the pressure-velocity coupling was achieved using the Semi-Implicit Method for Pressure-Linked Equations (SIMPLE) algorithm.⁽⁶⁶⁾ The convergence criterion for the continuity equation and momentum equation was 10^{-3} and the convergence criterion for the energy equation and the species transport equations was 10^{-6} . The species transport equations converged very slowly and results were monitored to ensure convergence of the ozone mass flow rate.

Computations were carried out on an IBM SP supercomputer and required about 150 hr CPU for each case.

3. MODELING RESULTS AND DISCUSSION

Distributions of O_3 and NO_x were obtained for six linear current densities (0.1, 1, 2.55, 5, 10, and $100 \mu\text{A}/\text{cm}$), six wire radii (10, 50, 100, 200, 500, and $1000 \mu\text{m}$), six temperatures (300, 400, 500, 600, 700, and 800 K) and six velocities (0.05, 0.1, 0.2, 0.5, 1, and 2 m/s). The time scales for production of ozone are discussed in Section 3.1. The insensitivity of production rate to changes in velocity is shown in Section 3.2. Relative production of O_3 and NO_x is discussed in Section 3.3. The effects of current density, wire radius, and temperature and comparison of numerical results with experimental data are presented in Sections 3.4 through 3.6.

3.1. Dominant Reactions and Their Time Scales

The dominant reactions, their relative contributions and characteristic times for the formation of O and O_3 and destruction of O_3 are listed in

Table II. The Dominant Reactions, Their Relative Contributions and Characteristic Times (τ) for the Formation of O and O₃ and Destruction of O₃^a

Formation of O			Formation of O ₃			Destruction of O ₃		
Reaction ^b	% ^c	τ (ms) ^d	Reaction	%	τ (ms)	Reaction	%	τ (ms)
23	62	7E-5	7	66	0.02	17	93	300
22	17	0.04	6	19	0.06	8	5	800
13	12	2	22	15	0.04	3e	2	4E-4
1e	7	7E-8	Total	100		Total	100	
15	1	3						
24	1	0.003						
Total	100							

^aThese values are calculated for the positive discharge from a 100 μm -radius wire operated at 300 K with a linear current density of 2.55 $\mu\text{A}/\text{cm}$ and bulk gas velocity of 0.5 m/s.

^bThe reaction number refers to the reaction listed in Table I.

^cThe relative contribution of the individual reaction to the formation/destruction of species is determined by the ratio of the volume-integrated rate of that reaction to the overall rate of formation/destruction of species over the volume.

^dThe characteristic time of a reaction is estimated as the reciprocal of the product of the rate coefficient and the maximum concentration of the major reactant (reactant with a higher concentration).

Table II for a 100 μm -radius wire operated at $I = 2.55 \mu\text{A}/\text{cm}$, $U = 0.5 \text{ m/s}$ and $T = 300 \text{ K}$. The relative contribution of an individual reaction to the formation/destruction of species is determined by the ratio of the volume-integrated rate of that reaction to the overall rate of formation/destruction of species over the volume. The relative contributions of individual reactions are nearly identical for the range of operating conditions considered. As expected, the formation of O and O₃ due to excited species (O₂^{*} and N₂^{*}) is significant. Half of the ozone is produced by N₂^{*} and nearly one-third is produced by O₂^{*}. The destruction of O₃ is primarily due to the generated NO (reaction 17).

Ozone is produced much faster than it is destroyed at the concentrations found in corona discharges in air. Thus, if the residence time of a device is larger than the characteristic time of the formation of O₃, the rate of production of O₃ is expected to be independent of velocity. Moreover, because the characteristic time of destruction of O₃ is much longer than the typical residence time, the net rate of ozone production is expected to remain constant far downstream of the discharge wire. Of course, the distribution of ozone within the flow channel is affected by the relative magnitude of transport by convection and diffusion. Studies that show the ozone production rate depends on velocity^(67,68) appear to have confused production rate with concentration. Obviously, for the same production rate, concentration decreases with increasing velocity. The characteristic time of a reaction is estimated as the reciprocal of the product of the rate coefficient and

the maximum concentration of the major reactant (reactant with a higher concentration). For reactions that produce O_3 , the major reactants are O_2 and N_2 and the estimated time scales depend only on temperature and pressure. The time scale for the formation of O_3 (reactions 6, 7, and 22) at 300 K is on the order of 0.01–0.1 ms. For reactions that destroy O_3 , the major reactant is O_3 , whose concentration depends on operating conditions. For the case shown in Table II, the time scale for the destruction of O_3 is several hundred milliseconds (reactions 3e, 8, and 17). For a highest current density of $100 \mu\text{A}/\text{cm}$, the time scale for destruction is on the order of 10 ms.

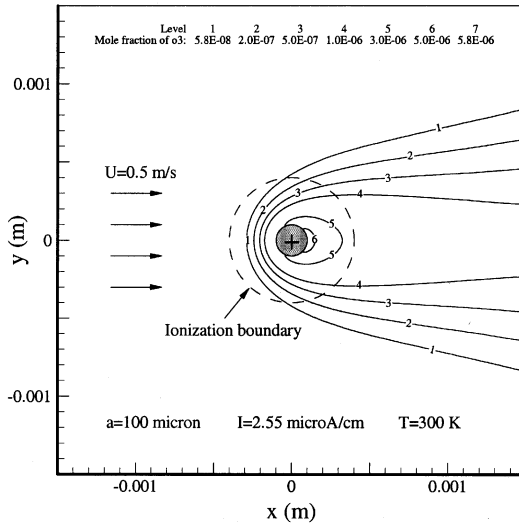
3.2. Effect of Velocity

To confirm our expectation and prior experimental studies^(22,28) that show ozone production is insensitive to gas velocity, we modeled a $100 \mu\text{m}$ -radius wire at $2.55 \mu\text{A}/\text{cm}$ for velocities ranging from 0.05 to 2 m/s. The corresponding residence times vary from 30 to 0.75 ms for a plate half-width of 0.15 cm. The distribution of ozone for $U = 0.5 \text{ m/s}$ and $U = 2 \text{ m/s}$ are plotted in Fig. 6(a) and (b). Contours of ozone mole fraction from the maximum to 1% of the maximum are shown. The legend indicates the value of each contour line. The dimensions of the computational domain, including the wire diameter and ionization region are indicated on the x - and y -axes. The dashed line is the location of the outside boundary of the plasma. The mass flow rate of any species j' ($m_{j'}$) across a cross-section at position x is calculated as

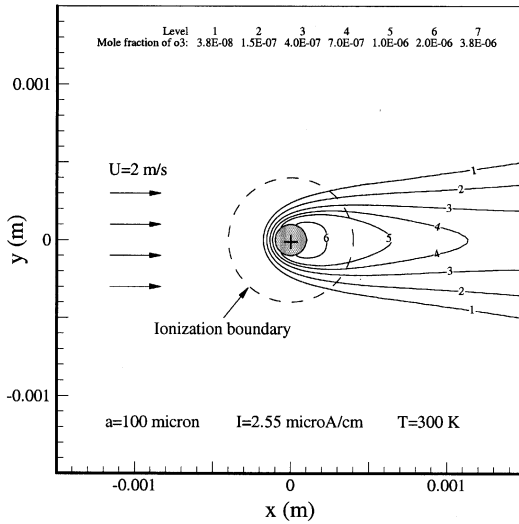
$$\dot{m}_{j'}|_x = \int_{-d}^d m_{j'} \rho v_x dy \quad (6)$$

Evaluation of this integral at the exit ($x = 0.0015 \text{ m}$) gives the overall production rate. For $U = 0.5 \text{ m/s}$, the maximum mole fraction is 5.8×10^{-6} and the production rate is $9.2 \times 10^{-4} \text{ mg/s-m}$ (expressed per unit length of wire). At $U = 2 \text{ m/s}$, the maximum mole fraction is 3.8×10^{-6} and the production rate is $8.7 \times 10^{-4} \text{ mg/s-m}$. The production rate at $U = 0.05 \text{ m/s}$ is $9.0 \times 10^{-4} \text{ mg/s-m}$ (not shown). The small variations in production rate with velocity are attributed to numerical uncertainty. With the increase of velocity, the residence time decreases and diffusion toward the plates is less significant.

In the remainder of this paper, we present results for a flow velocity of 0.5 m/s. Flow streamlines are plotted in Fig. 7 for a wire radius equal to $100 \mu\text{m}$. Again, the dashed circle indicates the location of the outer edge of the ionization region. Because the flow Reynolds number, based on wire diameter, is 6.3, the effect of the wire on the flow stream is minimal and constrained to the plasma region.



(a)



(b)

Fig. 6. Effect of velocity on ozone distribution for a 100 μm -radius wire at a current density of 2.55 $\mu\text{A}/\text{cm}$ and 300 K. (a) Contours of constant ozone mole fraction for $U = 0.5$ m/s. The rate of ozone production per unit length of wire is 9.2×10^{-4} mg/s-m. (b) $U = 2$ m/s. The rate of ozone production is 8.7×10^{-4} mg/s-m. The contour line corresponding to an ozone concentration at level 7 coincides with the downstream surface of the wire.

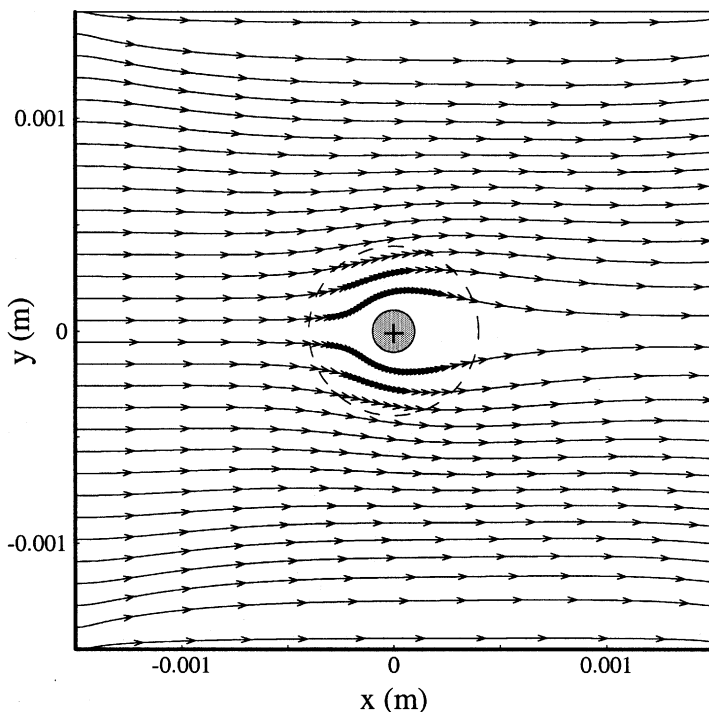


Fig. 7. Streamlines for flow transverse to a $100\ \mu\text{m}$ radius wire. The inlet velocity is $0.5\ \text{m/s}$. Reynolds number based on wire diameter is 6.3 . Arrows indicate the direction of velocity.

3.3. Relative Production of O_3 and NO_x

The mass flow rates of O_3 , NO , N_2O , NO_2 , NO_3 , and N_2O_5 from $x = -0.0004\ \text{m}$ (the upstream edge of the ionization region) to $x = 0.0015\ \text{m}$ (the outlet) are plotted in Fig. 8 for $a = 100\ \mu\text{m}$, $I = 2.55\ \mu\text{A/cm}$, and $T = 300\ \text{K}$. The plot illustrates the difference in production rates and allows interpretation of the effects of the relative magnitude of the characteristic times of formation and destruction.

Ozone production is significantly greater than the production of nitrogen oxides. NO and N_2O are major components of product NO_x ; however, the maximum concentration of NO ($0.12\ \text{ppm}$) is only 2% of that of O_3 ($5.8\ \text{ppm}$). The maximum concentration of N_2O ($0.028\ \text{ppm}$) is 0.5% of that of O_3 . The rates of production of NO and N_2O are $5.6 \times 10^{-5}\ \text{mg/s-m}$ (6% of O_3) and $3.6 \times 10^{-6}\ \text{mg/s-m}$ (0.4% of O_3), respectively. Production rates for NO_2 , NO_3 , and N_2O_5 are 3 to 12 orders of magnitude lower.

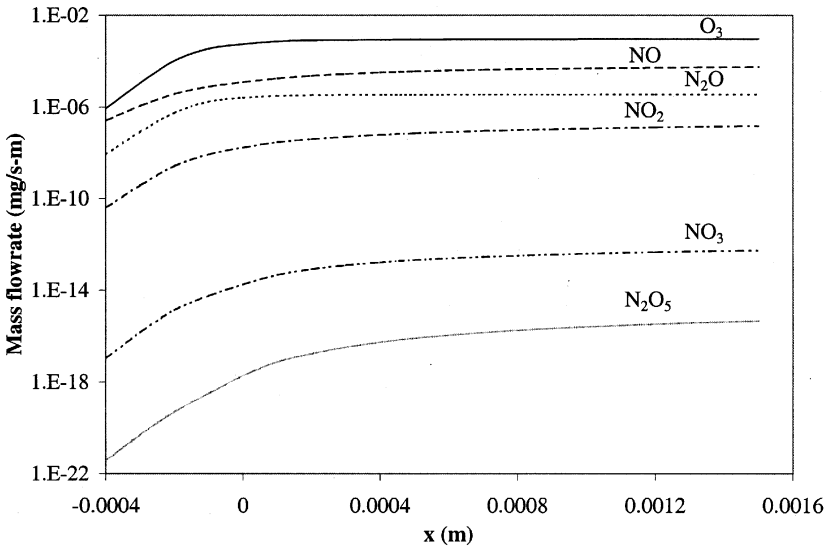


Fig. 8. Mass flow rates of O₃, NO, N₂O, NO₂, NO₃, and N₂O₅ are plotted as a function of streamwise position for $a = 100 \mu\text{m}$, $I = 2.55 \mu\text{A/cm}$, $U = 0.5 \text{ m/s}$, and $T = 300 \text{ K}$. The wire is centered at $x = 0 \text{ m}$. The corona plasma is a cylindrical sheath surrounding the wire with an outer radius of 0.0004 m .

The shape of the curves in Fig. 8 is a function of the characteristic times of formation and destruction. Formation prevails over the destruction of ozone inside the ionization region. The destruction balances the formation of ozone downstream of the ionization region. Thus, the ozone mass flow increases steeply from the front edge of the ionization region to just downstream of the center of the wire. It maintains a constant value on the order of $1 \times 10^{-3} \text{ mg/s-m}$ ($9.2 \times 10^{-4} \text{ mg/s-m}$) for all positions downstream of the ionization region ($x > 0.0004 \text{ m}$). These trends agree with those predicted by Peyroux⁽¹⁷⁾ for pulse discharges. The constant production rate for NO_x is reached further downstream of the wire because the formation of NO_x is slower than that of ozone. The residence time considered in this study is not long enough to reach chemical equilibrium. Eventually, the NO and NO₂ will be converted to N₂O₅ in the presence of O₃.

3.4. Effect of Current

The effect of current is evaluated for a $100 \mu\text{m}$ -radius wire. Linear current densities of 0.1, 1, 2.55, 5, 10, and $100 \mu\text{A/cm}$ are considered. These

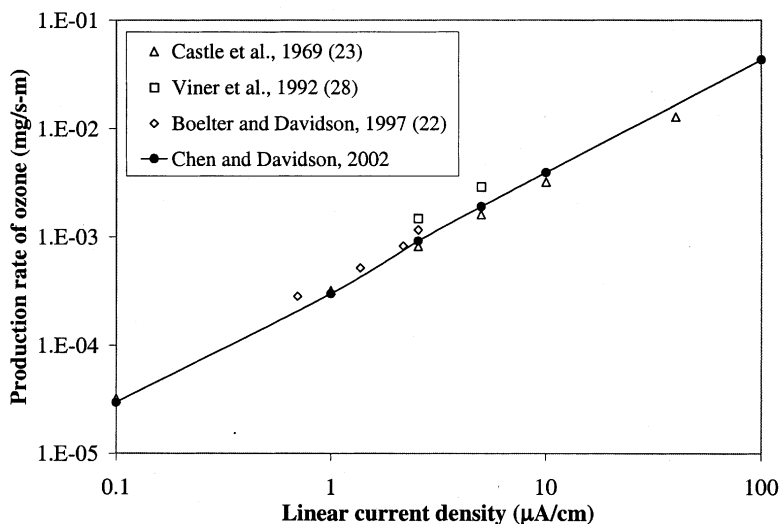


Fig. 9. Effect of current on the rate of production of ozone for $a = 100 \mu\text{m}$. The numerical results at $T = 300 \text{ K}$ and $U = 0.5 \text{ m/s}$ are compared to measured data. The data attributed to Castle *et al.*⁽²³⁾ and Viner *et al.*⁽²⁸⁾ are not measured directly but are determined from empirical correlations provided by the authors.

values span the practical range between corona onset and sparkover. Current affects the magnitude of the ozone concentration, but not the shape of the ozone distribution. A comparison of the predicted ozone production rate to experimental data is presented in Fig. 9. The data attributed to Castle *et al.*⁽²³⁾ and Viner *et al.*⁽²⁸⁾ are not measured directly but are determined from empirical correlations provided by the authors. There is excellent agreement of the predicted and measured values even though the data were measured in both wire-cylinder⁽²³⁾ and different wire-plate geometries,^(22,28) and in ambient air (as opposed to dry air). Ozone production increases linearly with current density due to the increase in electron number density. Current level does not affect the electron kinetic energy and rate coefficients for electron-impact reactions.

3.5. Effect of Wire Radius

The effect of wire radius is evaluated for radii equal to 10, 50, 100, 200, 500, and $1000 \mu\text{m}$. The surface current density (J) for all cases is set to 0.406 A/m^2 (equivalent to a linear current density $I = 2.55 \mu\text{A/cm}$ for $a =$

100 μm). The distributions of ozone for $a = 10 \mu\text{m}$ and $a = 1000 \mu\text{m}$ are plotted in Fig. 10(a) and (b). With an increase in wire radius, the plasma becomes thicker and more electrons are generated. Although electrons are less energy due to the lower electric field near the surface of the larger wires, the rate of production of ozone increases monotonically with wire radius. The relatively low concentration of ozone upstream of the wire and outside the boundary of the plasma is attributed to diffusion.

The rate of ozone production vs. wire radius is compared to experimental data in Fig. 11 for a fixed surface current density, air temperature and velocity. The data attributed to Castle *et al.*⁽²³⁾ and Viner *et al.*⁽²⁸⁾ are not measured directly but are determined from empirical correlations provided by the authors. The data attributed to Nashimoto⁽²⁵⁾ are the product of values read from his plot of ozone molar flow rate per unit current and total current. The data attributed to Awad and Castle⁽²¹⁾ are the product of values read from their table of ozone concentration per unit current, flow rate and total current. The agreement is excellent for wire radii greater than 50 μm . Nashimoto's⁽²⁵⁾ data for ozone production in a wire-plate geometry are higher than the predicted values. The discrepancy is possibly due to experimental pressures above atmospheric pressure. Electric field and the electron energy increase with increasing gas pressure.

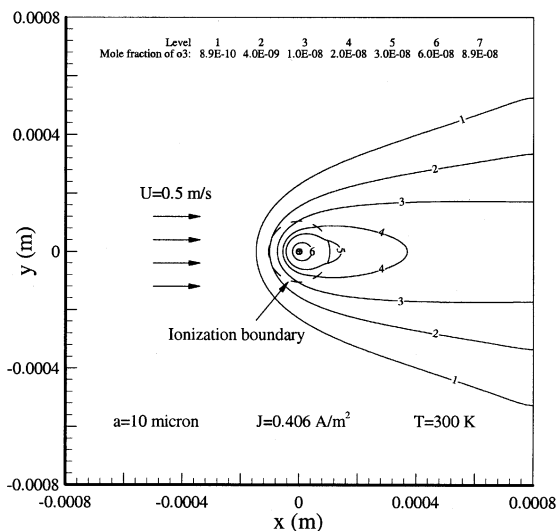
3.6. Effect of Temperature

Temperature affects the ozone generation through its effects on thermodynamic and transport properties and chemical reaction rates. The rate coefficients of electron-impact reactions increase with increasing temperature (see for example the dissociation of O_2 in Fig. 5). On the other hand, the gas density and the rates of endothermic reactions 6 and 7 that produce O_3 decrease. These competing effects are investigated for temperatures from 300 to 800 K for $a = 100 \mu\text{m}$, $I = 2.55 \mu\text{A}/\text{cm}$, and $U = 0.5 \text{ m/s}$.

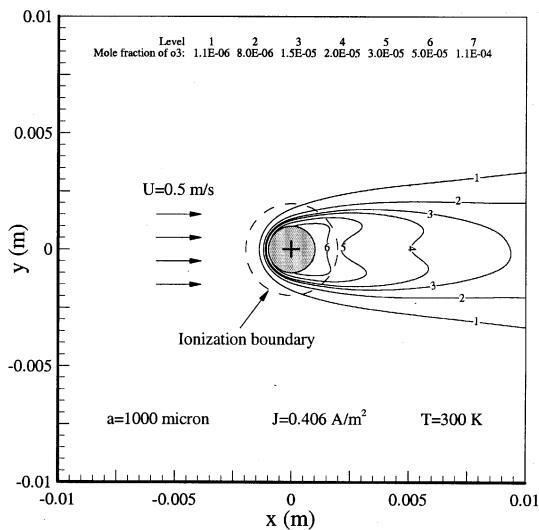
The distribution of ozone for the highest temperature ($T = 800 \text{ K}$) is plotted in Fig. 12. Compared with the ozone distribution at 300 K shown in Fig. 6(a), ozone is more dispersed within the flow channel due to an increase in diffusivity and the production rate is 79% lower. Figure 13 is a plot of ozone production rate vs. temperature. As temperature is increased, the rate of production of ozone decreases.

4. CONCLUSION

Electrons produced in corona discharges in atmospheric air initiate gas-phase reactions to produce O_3 and NO_x . A comprehensive numerical model is provided to predict the distribution as well as the rate of production of



(a)



(b)

Fig. 10. Effect of wire radius on ozone distribution for $J = 0.406$ A/m², $T = 300$ K, and $U = 0.5$ m/s. (a) Contours of constant ozone mole fraction for $a = 10$ μm . The plasma is 90 μm thick and the maximum ozone concentration is 89 ppb. (b) $a = 1000$ μm . The plasma is 968 μm thick and the maximum ozone concentration is 110 ppm. The contour line corresponding to an ozone concentration at level 7 coincides with the downstream surface of the wire.

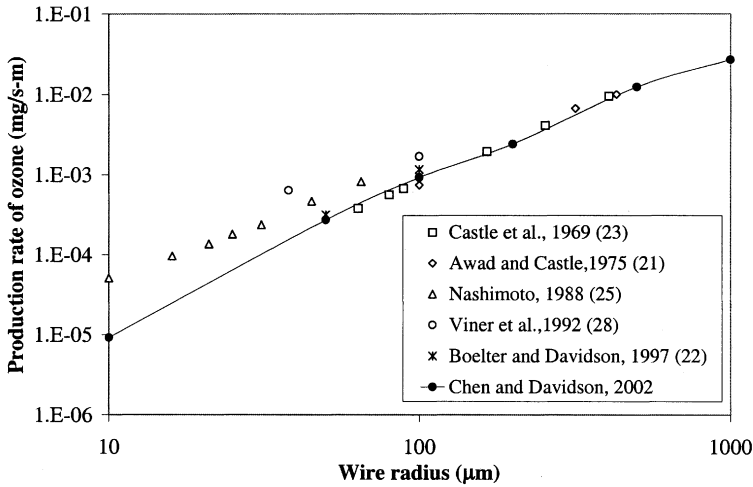


Fig. 11. Effect of wire radius on the rate of production of ozone for $J = 0.406 \text{ A/m}^2$. The numerical results at $T = 300 \text{ K}$ and $U = 0.5 \text{ m/s}$ are compared to measured data. The data attributed to Castle *et al.*⁽²³⁾ and Viner *et al.*⁽²⁸⁾ are not measured directly but are determined from empirical correlations provided by the authors. The data attributed to Nashimoto⁽²⁵⁾ are the product of values read from his plot of ozone molar flow rate per unit current and total current. The data attributed to Awad and Castle⁽²¹⁾ are the product of values read from their table of ozone concentration per unit current, flow rate, and total current.

gaseous species in the positive DC corona discharge. The model accounts for the spatial distributions of the number density and energy of electrons and reactions involving excited states of nitrogen and oxygen. It is validated with experimental data available in the literature.

Ozone production rate is 2 to 12 orders of magnitude greater than the production rate of NO_x . Reactions involving N_2^* and O_2^* serve as important pathways for ozone production in corona discharges. Half of the ozone is produced by N_2^* and nearly one-third is produced by O_2^* . Earlier models that neglected the excited molecular states are expected to under predict ozone production.

A study of the effects of current, wire radius, gas temperature, and gas velocity shows that current and wire radius have the most important impact. The rate of ozone production increases linearly with current for a fixed wire radius and temperature. At 300 K, ozone production rate can be reduced by 62% by using a 100 μm - rather than 200 μm -radius wire for surface current density equal to 0.406 A/m^2 . Small temperature fluctuations (e.g., within $\pm 10 \text{ K}$) near room temperature have negligible effect on the rate of ozone production. When temperature is increased from 300 to 500 K, the

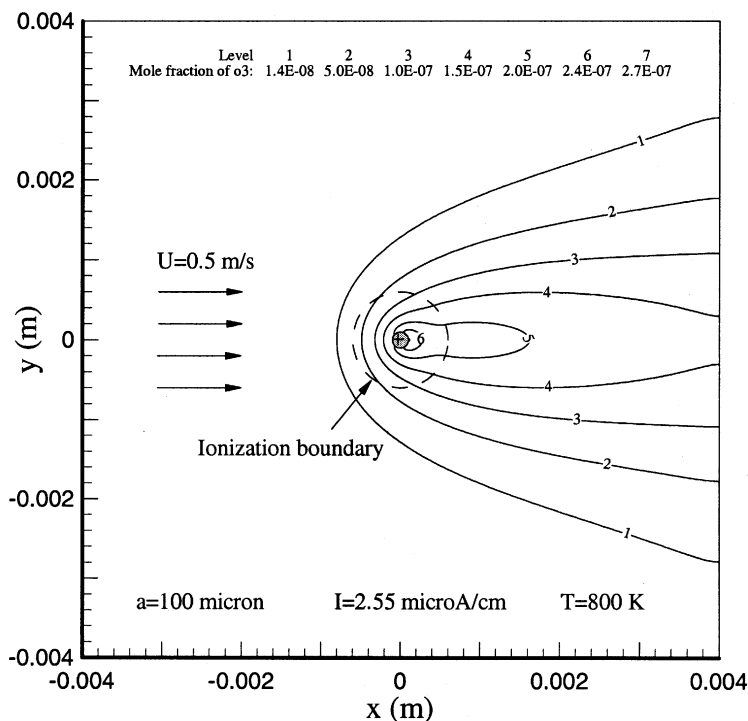


Fig. 12. Distribution of ozone for $a = 100 \mu\text{m}$, $I = 2.55 \mu\text{A/cm}$, $T = 800 \text{ K}$, and $U = 0.5 \text{ m/s}$. The plasma is $498 \mu\text{m}$ thick and the maximum ozone concentration is 0.27 ppm . The contour line corresponding to an ozone concentration at level 7 coincides with the downstream surface of the wire.

ozone production rate decreases by 44% for the $100\text{-}\mu\text{m}$ radius wire. Above 500 K , the rate of decrease with temperature is lower. Although the gas velocity affects the distribution of ozone, it has no effect on overall production for residence time from 0.75 to 30 ms and typical operating current ($2.55 \mu\text{A/cm}$) of corona devices because ozone is produced much faster than it is destroyed.

NOMENCLATURE

- σ collision cross-section, m^2
- τ characteristic time of the individual reaction, ms
- ρ gas density, kg/m^3
- a wire radius, cm

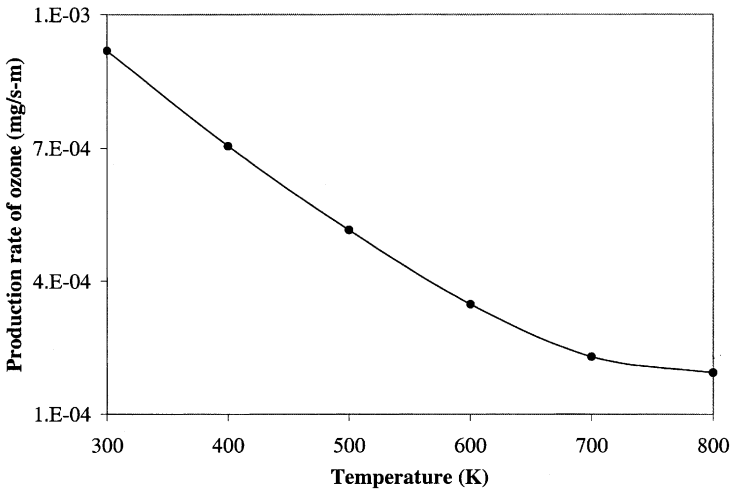


Fig. 13. Effect of temperature on the production rate of ozone for $a = 100 \mu\text{m}$, $I = 2.55 \mu\text{A/cm}$, and $U = 0.5 \text{ m/s}$.

- c_p specific heat at constant pressure, J/kg-K
 d wire-plate spacing, cm
 $D_{j'}$ dilute diffusion coefficient of species j' , m^2s^{-1}
 μ dynamic viscosity, kg/m-s
 e elementary charge, $1.6 \times 10^{-19} \text{ C}$
 E electric field, V/m
 f_0 electron energy distribution function, $\text{eV}^{-3/2}$
 g gravitational acceleration, m/s^2
 $h_{j'}$ specific enthalpy of species j' , J/kg
 $h_{j'}^0$ formation enthalpy of species j' , J/mol
 I linear current density, $\mu\text{A/cm}$
 J surface current density, A/m^2
 $J_{j'i}$ dilute diffusion flux of species j' , $\text{kg/m}^2\text{-s}$
 k_e rate coefficient of electron-impact reactions, m^3s^{-1}
 L total number of species
 m_e electron mass, $9.1 \times 10^{-31} \text{ kg}$
 $m_{j'}$ mass fraction of species j'
 $\dot{m}_{j'}$ mass flow rate of species j' per unit length of wire, mg/s-m
 $M_{j'}$ molecular weight of species j' , kg/mol
 N neutral density, m^{-3}
 p pressure, Pa
 $R_{j'}$ volumetric rate of creation/depletion of species j' , $\text{kg/m}^3\text{-s}$

T	temperature, K
λ	thermal conductivity, W/m-K
T_0	inlet air temperature, K
u	electron kinetic energy, eV
U	inlet air velocity, m/s
u_{th}	energy threshold for a reaction, eV
v_i, v_j	velocity, m/s; i and j are spatial indices
v_x	velocity in the x -direction, m/s
v_y	velocity in the y -direction, m/s
w	plate half-width, cm

ACKNOWLEDGMENTS

We would like to thank Dr. Michael Zachariah and Dr. Ulrich Kogelschatz for their helpful comments on the ozone chemistry and the Supercomputing Institute at the University of Minnesota for computational resources.

REFERENCES

1. H. Witschi, *Toxicology* **48**, 1–20 (1988).
2. M. Lippmann, *Air and Waste Management Assoc.* **39** (5), 672–694 (1989).
3. U.S. Environmental Protection Agency, *Health and Environmental Effects of Ground-Level Ozone*, <http://www.epa.gov> (2002).
4. American Lung Association, *Ozone Air Pollution*, <http://www.lungusa.org> (2002).
5. American Lung Association, *Recent Studies on the Health Effects of Air Pollution: Ozone Air Pollution*, <http://www.lungusa.org> (2002).
6. U.S. Environmental Protection Agency, *National 1-Hour Primary and Secondary Ambient Air Quality Standards for Ozone*, in *Code of Federal Regulations* (2001), Vol. 2, Title 40, Chapter I, Part 50, Sec. 50.9.
7. U.S. Department of Labor, Occupational Safety and Health Administration, *Limits for Air Contaminants: Toxic and Hazardous Substances*, in *Code of Federal Regulations* (2001), Vol. 6, Title 29, Chapter XVII, Part 1910, Subpart Z, Sec. 1910.1000, Table Z-1.
8. U.S. Department of Health and Human Services, Food and Drug Administration, *Maximum Acceptable Level of Ozone*, in *Code of Federal Regulations* (2001), Vol. 8, Title 21, Chapter I, Part 801, Sec.801.415, pp. 26–27.
9. R. G. Rice, *Ozone Science & Engineering* **18** (6), 477–515 (1997).
10. R. L. Laroque, *Ozone Science & Engineering* **21** (2), 119–125 (1999).
11. R. G. Rice, *Ozone Science & Engineering* **21** (2), 99–118 (1999).
12. R. G. Rice and A. Netzer, *Handbook of Ozone Technology and Applications*, (Ann Arbor, Mich., 1982).
13. B. Eliasson, M. Hirth, and U. Kogelschatz, *J. Phys. D: App. Phys.* **20**, 1421–1437 (1987).
14. R. Peyrous, P. Pignolet, and B. Held, *J. Phys. D: Appl. Phys.* **22**, 1658–1667 (1989).
15. B. Held and R. Peyrous, *Eur. Phys. J. AP* **4**, 73–86 (1998).
16. B. Held and R. Peyrous, *Eur. Phys. J. AP* **7**, 151–166 (1999).
17. R. Peyrous, *Ozone Science & Engineering* **12**, 41–64 (1990).

18. C. Monge, R. Peyrous, and B. Held, *Ozone Science & Engineering* **19**, 533–547 (1997).
19. V. G. Samoilovich and Y. V. Filippov, *Russian J. Phys. Chem.* **36** (7), 760–763 (1962).
20. J. L. Loiseau, F. Lacasse, C. Monge, R. Peyrous, B. Held and C. Coste, *J. Phys. D: Appl. Phys.* **27**, 63–73 (1994).
21. M. B. Awad and G. S. P. Castle, *J. Air Pollution Control Assoc.* **25** (4), 369–374 (1975).
22. K. Boelter and J. H. Davidson, *Aerosol Sci. and Tech.* **27** (6), 689–708 (1997).
23. G. S. P. Castle, I. I. Inculet, and K. I. Burgess, *IEEE Trans. Ind. Gen. Appl.* **IGA.5** (4), 489–496 (1969).
24. B. Held and R. Peyrous, *Czech. J. Phys.* **49**(3), 301–320 (1999).
25. K. Nashimoto, *J. Imaging Sci.* **32** (5), 205–210 (1988).
26. T. Ohkubo, S. Hamasaki, Y. Nomoto, J. S. Chang, and T. Adachi, *IEEE Trans. Ind. Appl.* **26** (3), 542–549 (1990).
27. S. Okazaki, H. Sugimitsu, H. Niwa, M. Kogoma, T. Moriwaki and T. Inomata, *Ozone Science & Engineering* **10**, 137–151 (1988).
28. A. S. Viner, P. A. Lawless, D. S. Ensor, and L. E. Sparks, *IEEE Trans. Ind. Appl.* **28** (3), 504–512 (1992).
29. R. Peyrous, C. Monge, and B. Held, *Ozone Science & Engineering* **20**, 317–342 (1998).
30. G. V. Naidis, *J. Phys. D: Appl. Phys.* **25**, 477–480 (1992).
31. S. Yagi and M. Tanaka, *J. Phys. D: Appl. Phys.* **12**, 1509–1520 (1979).
32. B. Eliasson and U. Kogelschatz, *J. Phys. B: At. Mol. Phys.* **19**, 1241–1247 (1986).
33. H. Sugimitsu and S. Okazaki, *J. Chimie Physique* **79** (9), 655–660 (1982).
34. B. Eliasson, U. Kogelschatz, and P. Baessler, *J. Phys. B: At. Mol. Phys.* **17** (22), L797–L801 (1984).
35. M. P. Iannuzzi, J. B. Jeffries, and F. Kaufman, *Chem. Phys. Lett.* **87**(6), 570–574 (1982).
36. A. R. De Sousa, M. Touzeau, and M. Petitdidier, *Chem. Phys. Lett.* **121**(4,5), 423–428 (1985).
37. M. P. Iannuzzi and F. Kaufman, *J. Phys. Chem.* **85**(15), 2163–2165 (1981).
38. V. Guerra, P. A. Sa, and J. Loureiro, *J. Phys. D: Appl. Phys.* **34**, 1745–1755 (2001).
39. B. Eliasson and U. Kogelschatz, *J. de Chimie Physique* **83**(4), 279–282 (1986).
40. D. Braun, U. Kuchler, and G. Pietsch, *J. Phys. D: Appl. Phys.* **24**(4), 564–572 (1991).
41. J. T. Herron, *J. Phys. Chem. Ref. Data* **28** (5), 1453 (1999).
42. J. T. Herron and D. S. Green, *Plasma Chem. and Plasma Proc.* **21** (3), 459–481 (2001).
43. I. A. Kossyi, A. Y. Kostinsky, A. A. Matveyev, and V. P. Silakkov, *Plasma Sources Sci. Technol.* **1** (3), 207–220 (1992).
44. FLUENT Inc., <http://www.fluent.com>
45. J. H. Davidson and E. J. Shaughnessy, *Exper. in Fluids* **4**, 17–26 (1986).
46. J. Chen and J. H. Davidson, *Plasma Chem. and Plasma Proc.* **22**(2), 199–224 (2002).
47. F. W. Peek, *Dielectric Phenomena in High-Voltage Engineering*, 3rd ed. (McGraw-Hill, New York, 1929).
48. J. J. Lowke and R. Morrow, *Pure & Appl. Chem.* **66**(6), 1287 (1994).
49. E. U. Condon and H. Odishaw, *Handbook of Physics* (McGraw-Hill, New York, 1967).
50. A. V. Phelps, *Compilation of Electron Cross Sections Used in JILA*, <ftp://jila.colorado.edu/collision—data/electron.txt>
51. R. D. Hudson, *Chlorofluoromethanes and the Stratosphere*, NASA Reference Publication 1010, (NASA, Washington, D.C., 1977).
52. R. F. Hampson and D. Garvin, *Chemical Kinetic and Photochemical Data for Modeling Atmospheric Chemistry* (U.S. Department of Commerce/National Bureau of Standards, Washington, D.C., 1975).
53. D. L. Baulch, R. A. Cox, R. F. Hampson, J. A. Kerr, J. Troe, and R. T. Watson, *J. Phys. Chem. Ref. Data* **9**, 295 (1980).

54. J. I. Steinfeld, S. M. Adler-Golden, and J. W. Gallagher, *J. Phys. Chem. Ref. Data* **16** (4), 911–951 (1987).
55. S. P. Sander, R. R. Friedl, W. B. DeMore, D. M. Golden, M. J. Kurylo, R. F. Hampson, R. E. Huie, G. K. Moortgat, A. R. Ravishankara, C. E. Kolb, and M. J. Molina, *Chemical Kinetics and Photochemical Data for Use in Stratospheric Modeling* (NASA Panel for Data Evaluation, Evaluation Number 13, 2000).
56. R. Atkinson, D. L. Baulch, R. A. Cox, R. F. Hampson, J. A. Kerr, M. J. Rossi, and J. Troe, *J. Phys. Chem. Ref. Data* **26** (3), 521 (1997).
57. R. Atkinson, D. L. Baulch, R. A. Cox, R. F. Hampson, J. A. Kerr, M. J. Rossi and J. Troe, *J. Phys. Chem. Ref. Data* **26** (6), 1329 (1997).
58. W. B. DeMore, S. P. Sander, D. M. Golden, R. F. Hampson, M. J. Kurylo, C. J. Howard, A. R. Ravishankara, C. E. Kolb, and M. J. Molina, *Chemical Kinetics and Photochemical Data for Use in Stratospheric Modeling* (NASA Panel for Data Evaluation, Evaluation Number 12, JPL Publication 97-4, 1997).
59. M. I. Boulos, P. Fauchais, and E. Pfender, *Thermal Plasmas: Fundamentals and Applications* (Plenum Press, New York, 1994).
60. S. W. Benson, *Adv. Chem. Ser.* **21**, 405 (1959).
61. P. C. Cosby, *J. Chem. Phys.* **98**(12), 9560–9569 (1993).
62. Yuri P. Riazar, *Gas Discharge Physics* (Springer, New York, 1997).
63. M. W. Chase, *NIST-JANAF Thermochemical Tables*, (American Chemical Society and the American Institute of Physics, 1998).
64. J. O. Hirschfelder, C. F. Curtiss, and R. B. Bird, *Molecular Theory of Gases and Liquids* (John Wiley & Son, Inc., New York, 1954).
65. R. J. Kee, R. M. Rupley, E. Meeks and J. A. Miller, *Chemkin-III: A Fortran Chemical Kinetics Package for the Analysis of Gas-Phase Chemical and Plasma Kinetic*, Sandia National Laboratories, Report No. SAND96-8216 (1996).
66. S. V. Patankar, *Numerical Heat Transfer and Fluid Flow* (Hemisphere, Washington, D.C., 1980).
67. M. Abdel-Salam, A. Mizuno, and K. Shimizu, *J. Phys. D: Appl. Phys.* **30**, 864 (1997).
68. A. Yehia, A. Mizuno, and K. Takashima, *J. Phys. D: Appl. Phys.* **33**, 2807 (2000).